Study of drag reduction using periodic spanwise grooves on incompressible viscous laminar flows

Pooyan Tirandazi and Carlos H. Hidrovo*
Mechanical and Industrial Engineering Department, Northeastern University, Boston, Massachusetts 02115, USA

(Received 26 March 2019; accepted 27 May 2020; published 22 June 2020)

Introducing surface corrugations to alter the boundary layer flow is a proven way to reduce the fluid drag on a surface. In this study, we examine the effect of periodic, infinitely long spanwise grooves on the laminar boundary layer over a plate for global Reynolds numbers (Re_L) between 1000 and 25 000. By employing numerical simulations in two-dimensional domains, we investigate the flow and pressure evolution over surfaces containing rectangular grooves that are perpendicular to the flow and infinitely long in the spanwise direction, and compare them to a flat plate. We characterize the flow interactions near the grooves based on their width-to-depth aspect ratio (AR). Below a certain aspect ratio, a primary vortex fills the space inside each groove. These vortices allow the free stream to "slip over" the grooved regions and result in less skin friction on the wall. However, the interaction between the flow and the grooves' vertical walls leads to a pressure drag. We study the behavior of the individual drag components over a wide range of aspect ratios ($0.2 < AR < 200$) and compare the total drag reduction in each case. Based on the simulation results, the transverse grooves in the laminar regime can reduce the total drag up to 10% in comparison to a flat plate, despite increasing the wetted surface area of the plate. Conversely, at some aspect ratios the grooves cause a total drag increase of more than 200%. We observe that by increasing the aspect ratio, the free stream bends more toward the grooves; ultimately at a certain aspect ratio, denoted by AR^*, the flow breaks apart the underlying circulation and reaches the bottom of the grooves. When this happens, the flow shear on the grooves' bottom walls combined with the high-pressure drag exerted on the vertical walls can lead to a net increase in the drag. Therefore, the aspect ratio of the grooves is a critical parameter in optimizing drag reduction in transverse geometries.

DOI: 10.1103/PhysRevFluids.5.064102

I. INTRODUCTION

The amount of drag force directly influences the energy required to flow fluids through channels and pipes or move objects within fluids. Therefore, finding strategies to reduce drag has potential industrial, environmental, and economic benefits. Several studies have repeatedly shown that adding different drag-reducing agents at the solid-liquid interface, such as polymers, surfactants, or air bubbles, reduces the drag by well above 50% in the turbulent regime [1,2]. While such active means provide a great improvement in the drag performance, continuous supply of the additive may not be practical for many applications. Moreover, additives can be a source of flow contamination and mechanical degradation of surfaces, which may necessitate performing postprocessing steps and consequently consuming additional energy and resources [2,3].

*hidrovo@northeastern.edu

Passive or geometrically mediated techniques have garnered a lot of interest in recent years. The fundamental idea behind passive methods is to utilize surfaces with irregular texturing or engineered micropatterns to reduce drag [4]. Observations of the natural surfaces of different animals and plants first inspired the use of surface topology methods, as in the case of drag-reducing shark skins or water-repellent lotus leaves [5,6]. Motivated by these observations, various forms of patterns, such as grooves (parallel or transverse), pillars, and holes, have been studied in terms of their drag-reducing ability and superhydrophobic action [7,8]. One way to lower the drag is to reduce the contact area of the fluid and the solid surface. Although introducing any corrugation on a simple flat plate will increase the overall surface area, one advantage of the textures is that they might entrap air within their structure. The underlying air pockets replace the liquid-solid interfaces with liquid-gas interfaces, which are believed to provide near shear-free regions and create an effective slippage for the flow [9]. This condition, which is typically referred to as the Cassie-Baxter state [10], is, however, easier said than done [11]. Creating and maintaining a stable gas-liquid interface is challenging as it requires careful design of the grooves and control of the flow to sustain the necessary capillary pressure across the interface [12–14]. This means that, on one hand, by making the grooves larger, the fraction of gas-liquid interface, and consequently the overall slippage, increases. On the other hand, enlarging the gas-liquid meniscus reduces the capillary pressure, which will eventually cause the air pockets to collapse, and thus results in a transition to the fully wetted Wenzel state. Furthermore, if the gas is soluble in the liquid (e.g., air in water), the gas pockets will gradually vanish as they dissolve in the liquid flow [15–17]. Similarly, the notion of the shear-free condition at the gas-liquid interface can be flawed as contamination may cause immobilization of the interface leading to a possible solidlike behavior [18–20].

The other advantage of the textured surfaces is their ability to induce unique near-wall flow fields that may ultimately reduce the overall drag on the surface even when the liquid is exposed to a larger wetted area. Early experiments by Walsh and co-workers [21–23] on longitudinal grooves demonstrated drag reduction in the turbulent regime ($<4\%$) despite increased surface area in comparison to a flat plate. Several studies since then have examined turbulent drag reduction using different riblet geometries and, with some variations, they have reported drag reductions of about 10% for open channel and 20% for closed channel experiments. Comprehensive reviews in the literature highlight the advances in turbulent drag reduction using longitudinal riblets in both external and internal flows [24,25]. Analysis of the flow field in streamwise riblets revealed that rib structures constrain the cross-flow fluctuations and lift the vortices that naturally occur in the turbulent regime so they have minimal contact with the surface [26–28]. Therefore, the ability of a riblet geometry to effectively uplift and pin the turbulent vortices on the riblet tips determines the amount of drag reduction. Fewer studies have considered the laminar boundary layer flow. Djenidi and colleagues [29] employed laser Doppler velocimetry and numerical simulations to study the laminar boundary layer over longitudinal rib surfaces with triangular geometry. They showed that despite the increased wetted area of ribbed surfaces, the net frictional drag did not change. Recent numerical analyses by Raayai-Ardakani and McKinley [30] examined the laminar boundary layer over wrinkled textures that feature periodic sinusoidal riblets in the flow direction. They demonstrated that in the valleys of the riblets the flow is retarded. Consequently, a stagnant cushion of fluid forms, above which the main flow can slip and exert as much as 20% less friction force on the wrinkled surface in comparison to a flat plate.

In contrast to the large amount of research associated with the flow dynamics of boundary layers over streamwise riblets, less is known regarding the effect of periodic spanwise riblets on the boundary layer flow and their drag characteristics. In the context of spanwise grooves, several studies have focused on the Cassie-Baxter state to reduce the solid-liquid contact area and create a superhydrophobic effect [31–37]. A few recent works on low-Reynolds number laminar microchannel flows ($\mathrm{Re} < 1000$) with wall-embedded grooves have reported that drag reduction may be obtained even in the fully wetted Wenzel state [18,38]. In pressure-driven channel flows, the drag is typically characterized by measuring the pressure drop along the channel, and the results are compared in terms of the Poiseuille number ($\mathrm{Po} = f\mathrm{Re}$) [18,39]. However, a clear understanding

of the local interaction of the grooves with the flow is still required, especially for medium- to high-Reynolds number laminar regimes.

Interactions of a fluid with rectangular grooves have also been studies in the context of flow inside and over cavities. Most of the research in this area either focused on solving the Stokes flow within cavities or investigated the turbulent boundary layer over a single embedded cavity [40,41]. Aerodynamic studies on cavity flows have shown that flow past cavities is likely to oscillate. Such oscillations can produce substantial aerodynamic drag and acoustic emissions, and their onset is typically characterized by dimensionless parameters D/θ_0 and $L/\theta_0\sqrt{\mathrm{Re}_{\theta_0}}$, where D and L are the cavity dimensions and θ_0 is the incoming momentum thickness [42–44]. Gatski and Grosch [45] numerically solved the two-dimensional boundary layer flow over a single rectangular cavity at lower cavity Reynolds numbers where no oscillations are present, and compared it to a flat plate. They argued that although the presence of a cavity region would reduce the frictional drag, the increase in the pressure forces acting on the vertical walls of the cavity almost cancels out this reduction and therefore causes less than 2.5% total drag reduction. There is still a lack of understanding regarding the evolution of the laminar flow over consecutive transverse grooves, which resemble periodic cavities that are infinitely extended perpendicular to the flow.

In this paper we explore the two-dimensional development of laminar flow over plates with embedded periodic transverse grooves assuming infinite span length in the third dimension. We perform finite element simulations over an array of equally spaced rectangular grooves and explore the velocity profile and boundary layer evolution for different groove dimensions in the laminar regime, where $1000 \leqslant \mathrm{Re}_L \leqslant 25\,000$ and the flow mainly remains steady. By examining the local shear stresses and pressures, we then focus on understanding the role that the skin friction and pressure play in the overall drag and ultimately determine the total drag reduction in comparison to a simple flat plate. We show that the width-to-depth aspect ratio (AR) of the trenches is a crucial parameter in determining the flow behavior in the grooves and their drag-reducing or -increasing ability. Below a certain AR, formation of a circulating flow within the grooves creates a "fluid bearing" [46] effect on the main flow resulting in less skin friction. However, unlike streamwise riblets, in transverse grooves the pressure drag plays an equally important role in the total drag. For the groove dimensions and Re_L considered in this study, certain configurations result in a drag reduction as high as 10%, whereas in other cases, the combination of skin friction and pressure causes a drag increase of more than 200%. We consider the laminar regime, focusing on the cases where no turbulence or acoustic effects are present, to acquire a foundational understanding of the flow interactions with the grooves for a wide range of groove dimensions, and to examine the interplay of skin friction and pressure drags. This is of direct benefit to the study of laminar boundary layer characteristics and optimization of the drag for airfoils, hydrofoils, and underwater surfaces, with direct applications in unmanned underwater vehicles (UUVs) or underwater drones, among others, where the laminar regime predominates [47–49]. The understandings gained here can also be expanded to other laminar flow systems, namely, in designing microfluidic platforms for microelectronic cooling and lab-on-a-chip applications. Furthermore, this work would also be relevant under mixed boundary layer conditions, where the flow might stay laminar and locally steady upstream and transition to unsteady and turbulent behavior downstream.

II. NUMERICAL METHODOLOGY

A. Computational setup and boundary conditions

The computational domain and the boundary conditions are shown schematically in Fig. 1. We consider cases where the third dimension extends infinitely in the third dimension. Therefore, we simulate the flow in two-dimensional domains. The flow enters the domain from the left with a uniform velocity condition (U). The inlet velocity is changed to obtain different Reynolds numbers in the simulations. The top and right boundaries are set as outlet with zero gauge pressure and zero velocity gradient across the boundary. The bottom edge of the domain is divided between the

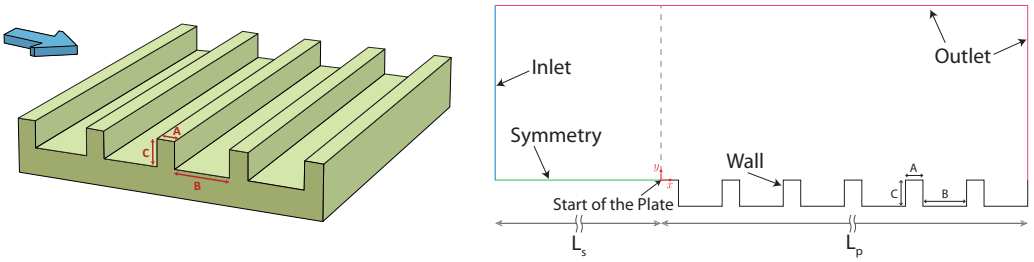

FIG. 1. (Left) Schematic of the plate with embedded grooves. The grooves are oriented perpendicularly to the flow direction which is shown by the arrow. (Right) Schematic of the simulation domain with the boundary conditions. We consider transverse grooves that are embedded in the plate with no protrusion into the main flow, and extend infinitely into the plane. As a result, a two-dimensional model is used to investigate the flow dynamics and drag properties.

grooved plate, which is modeled as a no-slip boundary condition, and an intermediate region with symmetry condition. The major role of the symmetry condition is to allow the numerical solver to properly resolve the leading-edge effects of the plate. More details on the effect of the symmetry region are provided in the following section. The domain height (H) is extended such that it covers at least $5\delta_L$ for all the flow conditions, where δ_L is the boundary layer thickness at the end of the plate. In this study, we only consider grooves or trenches with rectangular profiles that are characterized by three parameters: A, which represents the distance between each two consecutive grooves (the width of each land segment of the plate at $y = 0$), and B and C, which show the grooves' width and depth (also referred to as valley segments of the plate), respectively. We refer to the depth of the grooves instead of their height to emphasize the fact that the grooves are embedded in the plate with zero protrusion into the main flow. The simulated plate in this study has a nominal length of $L_p = 96\,\text{mm}$. The width of the land regions is constant ($A = 1\,\text{mm}$) throughout the simulations, and we only change B and C to obtain different texture configurations. The value of B is systematically increased such that there is a valley for every land segment within the domain. Therefore, B takes the values of 1, 2, 3, 5, 7, 11, 23, 47, and 95 mm. By considering four different depths (0.5, 1, 2, and 4 mm), 36 different combinations of groove depths and widths are simulated at each Re_L. Throughout this work, we use two nondimensional parameters to characterize the grooves and their drag behavior at each Re_L; AR, which is the grooves' aspect ratio and is defined as B/C, and ε, which shows a "relative roughness" for the textured plates and is defined as C/L_p.

The numerical solution of the Navier-Stokes equations is used to obtain the fluid velocity and pressure fields in the computational domain assuming a laminar flow. The simulations are performed in a transient manner and the drag forces on the plate are monitored throughout the run. For most of the groove dimensions and flow parameters considered in this work, the drag force reached a plateau after a few seconds, indicating a steady flow situation. We realized that at higher Re_L, as grooves become larger, the flow shows an oscillating behavior that causes the drag forces to fluctuate over time. In this situation, the time-averaged drag is used to compare the grooves' performance. We will discuss some of these phenomena and the consequences of the unsteady effects on the drag magnitude. We use a finite element scheme for discretizing the conservation equations and coupling the pressure and velocity. The working fluid in the simulations is assumed to be liquid water at room temperature and atmospheric pressure with $\rho = 998.2\,\text{kg/m}^3$ and $\mu = 1.003 \times 10^{-3}\,\text{kg/m s}$.

III. MODEL VALIDATION

A grid-independence study was performed by stepwise refinement of the elements, especially close to the wall boundaries, inside the trench regions, and close to the leading edge of the plate.

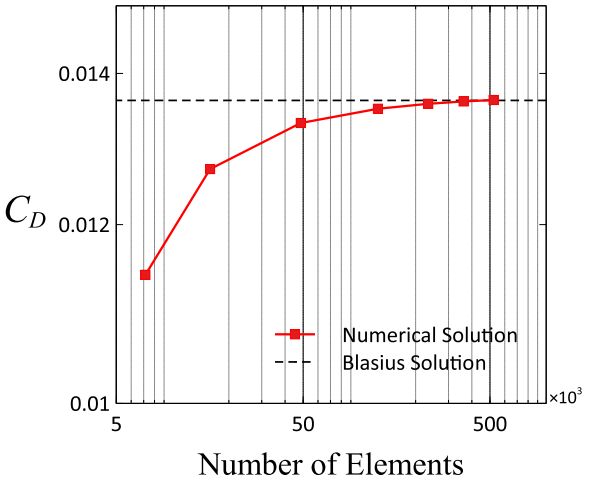

FIG. 2. The influence of the number of elements in the computational grid on the drag coefficient of a flat plate (C_D) at $\mathrm{Re}_L \approx 10^4$. The dashed line represents the value obtained from the Blasius solution ($1.328/\sqrt{\mathrm{Re}_L} \approx 0.0136$).

The final mesh consists of elements as small as $0.0001L_p(\sim 10\,\mu\mathrm{m})$ near the plate boundary and reaching up to $0.005L_p(\sim 500\,\mu\mathrm{m})$along the top edge of the domain ($y = H$). Figure 2 shows the behavior of the drag coefficient of a flat plate at $\mathrm{Re}_L \approx 10^4$ based on the total number of elements in the computational domain. We should note that since the simulations are performed on a two-dimensional domain, the forces are calculated by integrating the local stresses along a line and thus have a unit of N/m. The numerical values of C_D are compared against the Blasius solution ($1.328/\sqrt{\mathrm{Re}_L}$) to ensure less than 1% error. For the textured plates, the elements are refined until the drag coefficient shows negligible difference upon further refinement, resulting in computational domains that contain above 1 000 000 elements in some cases.

The role of the entry region in the simulations is critical for properly resolving the evolution of pressure and velocity over the plate. Figure 3 shows the pressure contours and velocity profiles for two cases, one without a symmetry section and one with the intermediate symmetry section. The leading-edge effects in the former case are forced to propagate in the plate direction. Consequently, we can see a favorable pressure gradient over the initial portion of the plate without the entry region, which deviates from the assumption of zero-pressure gradient in external flow over a flat surface. Extending the simulation domain upstream of the plate allows the numerical solver to better resolve the spatial pressure and velocity fields over the plate and, thus, confine the leading-edge effects to a significantly smaller portion of the plate. Similarly, the nondimensional velocity profiles along the plate are compared for the two cases. We plot the Blasius similarity variable, $\eta = y\sqrt{U/\nu x}$, against the nondimensional velocity in the x direction (u/U) at different local Reynolds numbers (Re_x). For a plate preceded by a symmetry region, the velocity profiles are self-similar and precisely follow the Blasius solution, whereas excluding this region results in higher velocities that are not similar and are higher than the free-stream velocity in some locations, which can be recognized by an overshoot in the profile. Therefore, including this region before the plate is essential for obtaining accurate pressure and velocity fields and ultimately calculating the drag coefficients.

Figure 4 shows the drag coefficient for a flat plate as the length of the entry region increases. It can be seen that at zero entry length, the drag coefficient of the flat plate is more than 40% higher than the Blasius solution. This difference can be associated with the leading-edge effects on the pressure and velocity fields that propagate in the plate direction. As the domain extends further

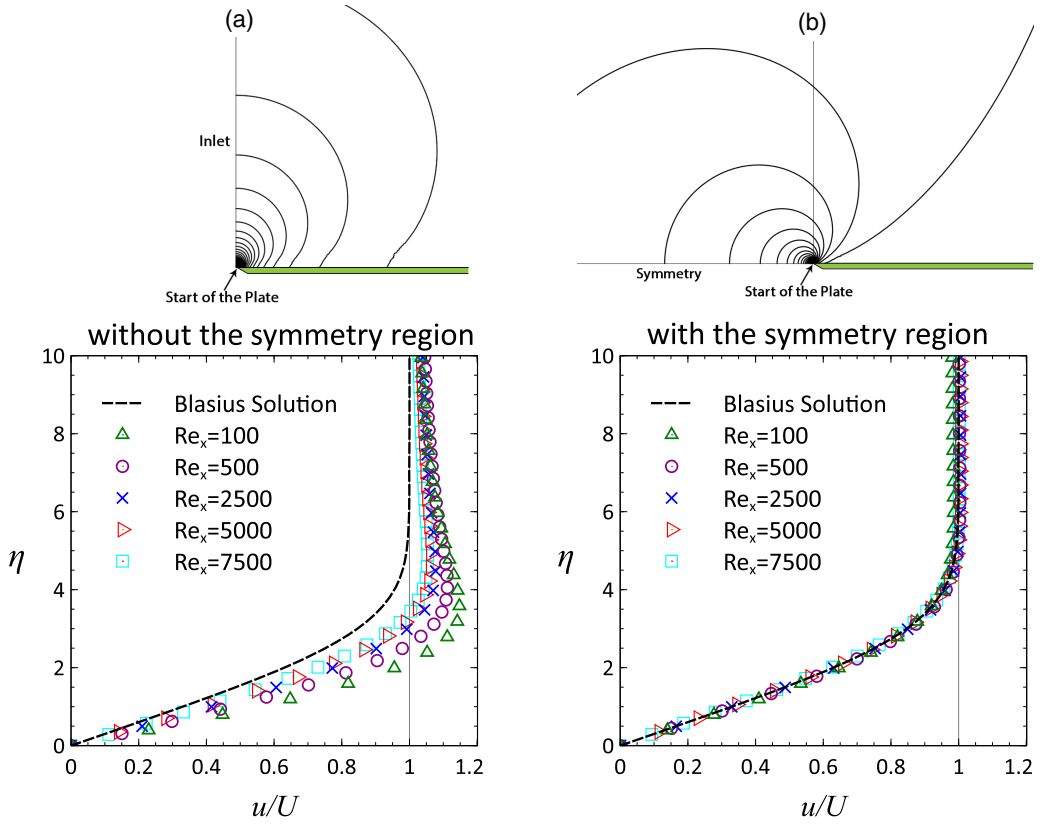

FIG. 3. Isopressure contours at the leading edge of a flat plate and nondimensional velocity profiles at different locations along the plate for (a) a domain without the symmetry region and (b) a domain with the symmetry region. Without such region, the leading-edge effects are propagated in the plate direction, causing a pressure gradient along the plate. By extending the domain prior to the plate, the pressure effects of the leading edge are impeded in the plate direction and instead, they propagate backward. $\eta = y/x\sqrt{\mathrm{Re}_x}$ represents the similarity variable in the Blasius solution. For a computational domain without the symmetry region the profiles deviate from the Blasius solution, especially as they get closer to the leading edge of the plate. The velocity profiles over a plate that is preceded by a symmetry region precisely follow the Blasius solution.

upstream, the value of C_D declines. For the computational parameters in this study, an entry region with almost the same length as the plate is required to fully incorporate the leading-edge effects and achieve accurate C_D within 1% of the Blasius solution.

We assume the transverse trenches in this study extend infinitely into the plane (i.e., very large span dimension relative to the plate length and groove dimensions). The effects of shorter grooves, whose span is of the same order as the plate length or the grooves' dimensions, are not considered in this paper. To ensure the absence of three-dimensional effects for the conditions of this work, we have cross-checked the cases with the biggest AR and ε that show drag reduction, against three-dimensional domains of the same grooves' layout, with the third dimension extending ten times the groove's depth (please refer to the Supplemental Material for a detailed discussion on three-dimensional model verification [50]). The results show very similar velocity and pressure fields, leading to close drag characteristics with less than 2.5% difference between two- and three-dimensional cases (when calculated per unit length of the third dimension). Furthermore, considering the low cavity Reynolds and Mach numbers in the current work ($\mathrm{Re}_C < 1000$ and $\mathrm{Ma} \ll 0.1$), the parameter window of the simulations falls in the two-dimensional (2D) stable regime

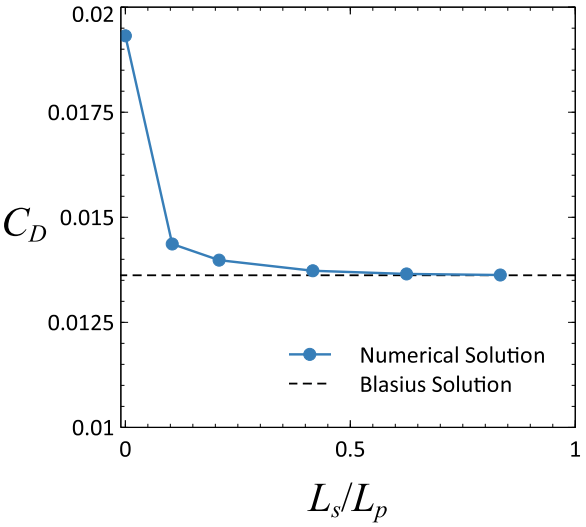

FIG. 4. The effect of the extended symmetry region length over the plate length (L_s/L_p) on the drag coefficient (C_D) at $\mathrm{Re}_L \approx 10^4$. To get accurate drag coefficients that are within 1% of the Blasius solution, an entry length of almost the same size as the plate is required for the simulations.

of the instability map for cavity flows [43,51]. Thus, we focus on two-dimensional domains to study the interaction of pressure and velocity in the grooves, and to ultimately calculate the different drag components.

IV. RESULTS AND DISCUSSIONS

A. Flow streamlines

We first explore the characteristics of the flow in the presence of the grooves by looking at the streamlines inside the grooves for different aspect ratios (ARs). Figure 5 illustrates the steady flow streamlines inside the first groove in the plate for selected ARs and two different orders of Re_L. We can identify circulating flow structures within the grooves, which are induced by the external motion of the fluid over the plate. For grooves with relatively equal width and depth (AR $\approx$ 1), a primary recirculation zone encompasses most of the interior region of the groove. In addition to this main circulation, there are much smaller eddies at the front and rear corner of the trench, which have been theoretically shown to consist of an infinite sequence of counter-rotating vortices [52]. When the groove's depth is greater than its width, the corner vortices, both of which rotate opposite to the main circulation, grow and merge to form a second vortex below the first one. For instance, for grooves with AR = 0.5, we see a dual counter-rotating structure. As AR decreases further, several additional circulation zones may grow and form in a similar fashion. In these stacked vortical structures, each two adjacent vortices rotate in opposite directions to conserve mass inside the groove, and the vorticity magnitude of the underlying vortices rapidly decreases with depth.

If the width of the groove increases relative to its depth, the primary vortex first stretches with its center shifting in the flow direction. At larger ARs, the free stream starts to deflect toward the trench region, and the inertia of the flow pushes the underlying circulation to the sides. Eventually, the streamlines bend enough that they reach the bottom of the trench. As a result, the main circulation is split into two triangular vortices at the front and rear corners. We can identify similar flow patterns inside the grooves with close values of AR despite having different widths and depths (see AR = 3–3.5 or AR = 5.5–5.75 in Fig. 5). Moreover, we observe that the collapse of the primary vortex

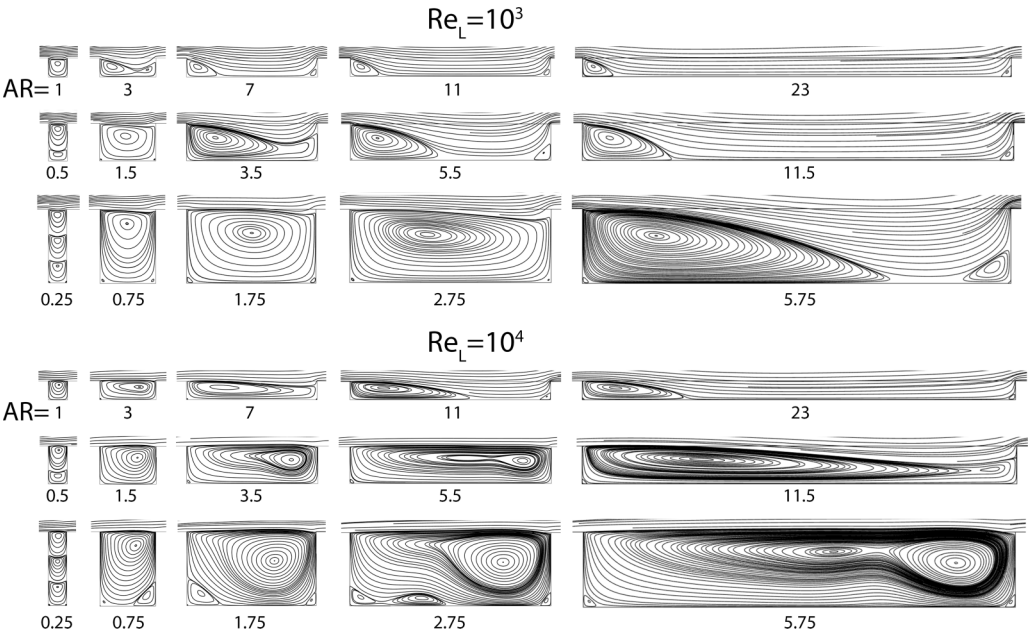

FIG. 5. Steady streamline patterns in the first groove of the periodic textures for different aspect ratios (AR) at $\mathrm{Re}_L \approx 10^3$ and $\mathrm{Re}_L \approx 10^4$. The behavior of streamlines can be classified into two major types. At smaller ARs, a primary circulation fills the groove and the free stream slips over the grooves. At larger ARs, the flow starts penetrating the grooves and eventually reaches the bottom of the grooves. In this state, the underlying vortex is split into two smaller vortices. We use AR^* to show the critical aspect ratio beyond which the flow fully penetrates the groove. As the Re_L increases, this transition occurs at higher ARs.

happens at about the same AR for grooves with different depths and widths. This indicates the significance of the AR as a crucial geometric parameter that should be used to characterize the flow patterns inside the grooves. Throughout this paper, we refer to AR^* as the aspect ratio where this transition takes place. We should note that since the values of AR increase in finite, discrete steps, AR^* takes on an approximate value. The streamline contours show that AR^* at $\mathrm{Re}_L \approx 10^3$ and 10^4 happens at about 5 and 11, respectively.

Each groove can be considered as a rectangular cavity in the flow. As suggested by the previous studies on flow over single cavities, it is therefore, crucial to investigate the possible oscillations that may occur in the flow, and their effect on the resultant drag. Figure 6 shows the unsteady streamlines for two different ARs. We can notice unsteady vortices that are confined to the grooves and show a repeating behavior at smaller AR. At larger ARs, however, the interaction of the flow with the trailing wall of the groove, which acts as a blunt body, causes a vortex shedding pattern. In this case, the oscillatory behavior of the vortices smore unpredictable as they not only propagate forward, but also travel out of the grooves in the main flow. The simulations maintained a steady behavior for all the groove dimensions at $\mathrm{Re}_L \approx 10^3$. Starting at $\mathrm{Re}_L \approx 10^4$, flow oscillations emerge in the grooves with larger AR and ε. The onset of the oscillations requires a minimum AR and ε, beyond which the flow transitions to the unsteady mode, also known as shear-layer or Rossiter mode [53]. As the Re_L increases, the transition from steady to oscillatory flow happens at smaller AR and ε and, thus, more cases fall in the unsteady regime. The onset of fluctuations over a single cavity is typically characterized by C/θ_0 and $B/\theta_0\sqrt{\mathrm{Re}_{\theta_0}}$ [42] (e.g., in our simulations the transition happens when $C/\theta_0 >\sim 45$ and $B/\theta_0\sqrt{\mathrm{Re}_{\theta_0}} >\sim 1150$). However, these parameters only consider the approaching boundary layer to the first groove and as such, do not provide a comprehensive view of the flow behavior over multiple grooves and their drag reduction mechanism, which is

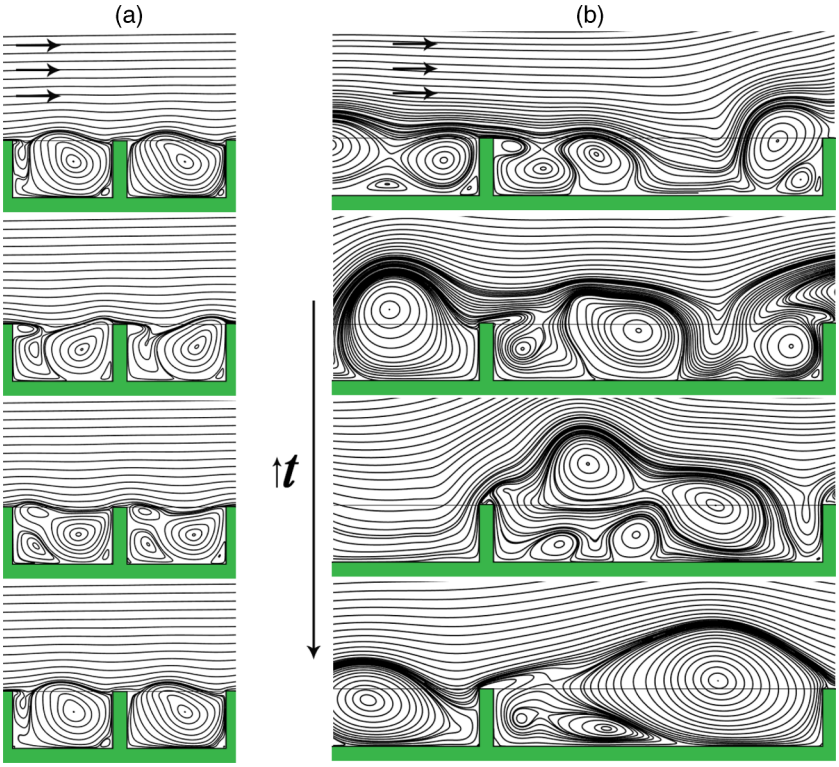

FIG. 6. Unsteady streamline patterns at $\mathrm{Re}_L \approx 2.5 \times 10^4$. (a) At smaller AR, the streamlines show a periodic behavior where the patterns are repeated over time. (b) At larger AR, the streamline patterns become more unpredictable as the interaction of the flow and the grooves' trailing walls causes vortex shedding inside and above the grooves.

the major goal in this work. Therefore, we use Re_L, AR, and ε to better assess the drag reduction over consecutive grooves (please refer to the Supplemental Material for a detailed map that shows the steady and unsteady regions considering both sets of parameters [50]). Eventually, at higher Re_L conditions ($\gtrsim 5 \times 10^4$), the unsteady behavior becomes more prevalent in the simulations, which are generally associated with substantial increase in the drag in comparison to a flat plate. Those cases are not the main focus of this work and, as such, we consider the grooved plates up to $\mathrm{Re}_L \approx 2.5 \times 10^4$, where steady behavior still dominates, and the majority of the cases show drag reduction.

The motion of the fluid over the plate creates vortices in the grooves which in turn give rise to a lift force that is proportional to the magnitude of their circulation. The streamline patterns show that these vortical structures act like a virtual wall under the main flow with a finite velocity at the interface and are able to "hold" the free stream and prevent it from penetrating. In Fig. 7 we look at the y direction force on a control volume that surrounds the flow within the grooves. The resultant vertical force on the fluid comes from the reaction of the shear on the side walls of the groove and the net fluid pressure in the vertical direction. To compare the lifting effects among different grooves, we calculate the force per width of the grooves (which is effectively the average lifting pressure) and normalize it against the dynamic pressure of the main flow ($\rho U^2/2$). The positive values of the plot indicate the upward reaction of the vortical flow. The conservation of momentum requires the net momentum outflux of the control volume to also be positive. As AR increases, streamlines deflect more, and their net momentum per trench width also increases until the flow reaches the bottom

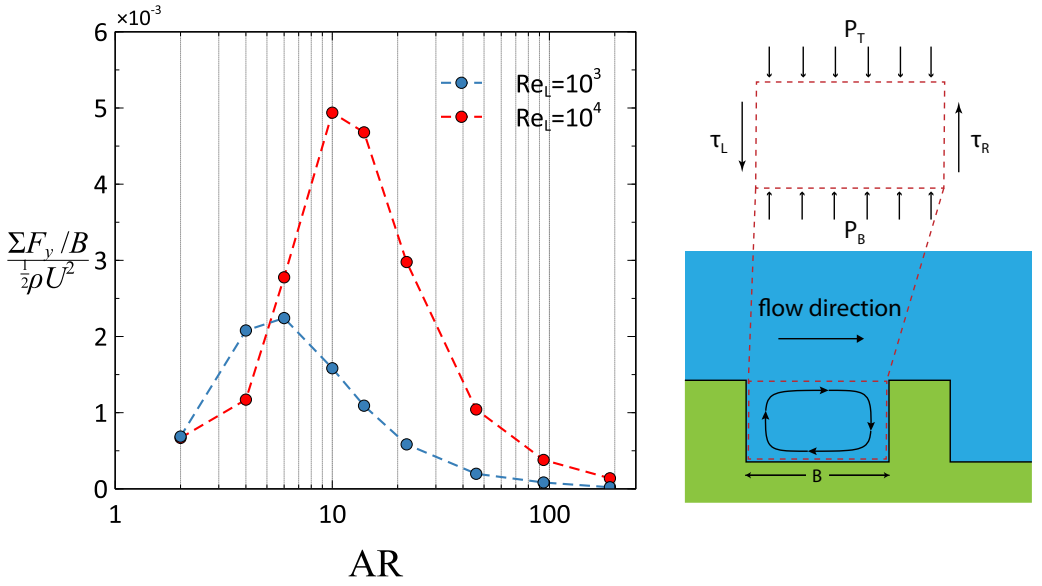

FIG. 7. Effect of the vortical flows in the grooves on their average lifting pressure for different aspect ratios (AR) and global Reynolds numbers (Re_L). The location of the maximum for each curve corresponds to the AR^* at that Re_L. After this point, the inertia of the main flow breaks apart the main vortex, causing a reduction in the net force per width of the vortices. At higher Re_L, the flow induces vortices with stronger circulations which improves the ability of the grooves for holding the main flow up to larger AR.

of the grooves. The location of the maximum in each curve corresponds to the AR^* for that Re_L where the main flow breaks apart the primary vortex. After this point, as the trench gets wider, the action of the vortices is restricted to the corners. Therefore, the average lifting pressure decreases. At higher Re_L, the maximum point of the plot shifts to larger values of AR, confirming the behavior of streamlines in Fig. 5. Here the induced vortices have stronger circulations that can sustain the flow up to larger ARs.

B. Velocity profiles

To better understand the velocity evolution within and over the grooves, it is important to look at the velocity profiles in the presence of a groove and compare them with the profile of the flat plate. Figure 8 shows the nondimensional velocity profiles for a single trench for relatively narrow and wide grooves (AR = 3 and 23) over two different Re_L. The horizontal axis shows the nondimensional velocity in the x direction with respect to the free-stream velocity (u/U), and the vertical axis shows the Blasius similarity variable $\eta = y\sqrt{U/\nu x}$. η takes positive values in the mainstream region above the grooves, whereas $\eta < 0$ corresponds to the portion of the velocity profiles inside the groove. The profiles are plotted at different locations along the trench, represented by a dimensionless length scale, $0 \leqslant \chi \leqslant 1$, where $\chi = 0$ marks the start of the groove and $\chi = 1$ corresponds to the end of the groove. The flow inside the grooves with $\mathrm{AR} < \mathrm{AR}^*$ consists of a primary circulation zone. Therefore, the velocity profiles at the bottom of the trench show a backward trend with negative values, which are at least an order of magnitude smaller than the free-stream velocity. At lower Re_L, the induced circulation and the backward motion are weaker at the bottom, and the flow inside the groove acts almost like a cushion of stagnant fluid with a resultant "slip velocity" at its interface with the free stream (see the plot for AR = 3 at $\mathrm{Re}_L = 10^3$). Increasing the Re_L induces a stronger circulation with bigger backward motion at the bottom of the trench. Accordingly, the bottom wall experiences a shear force opposite to

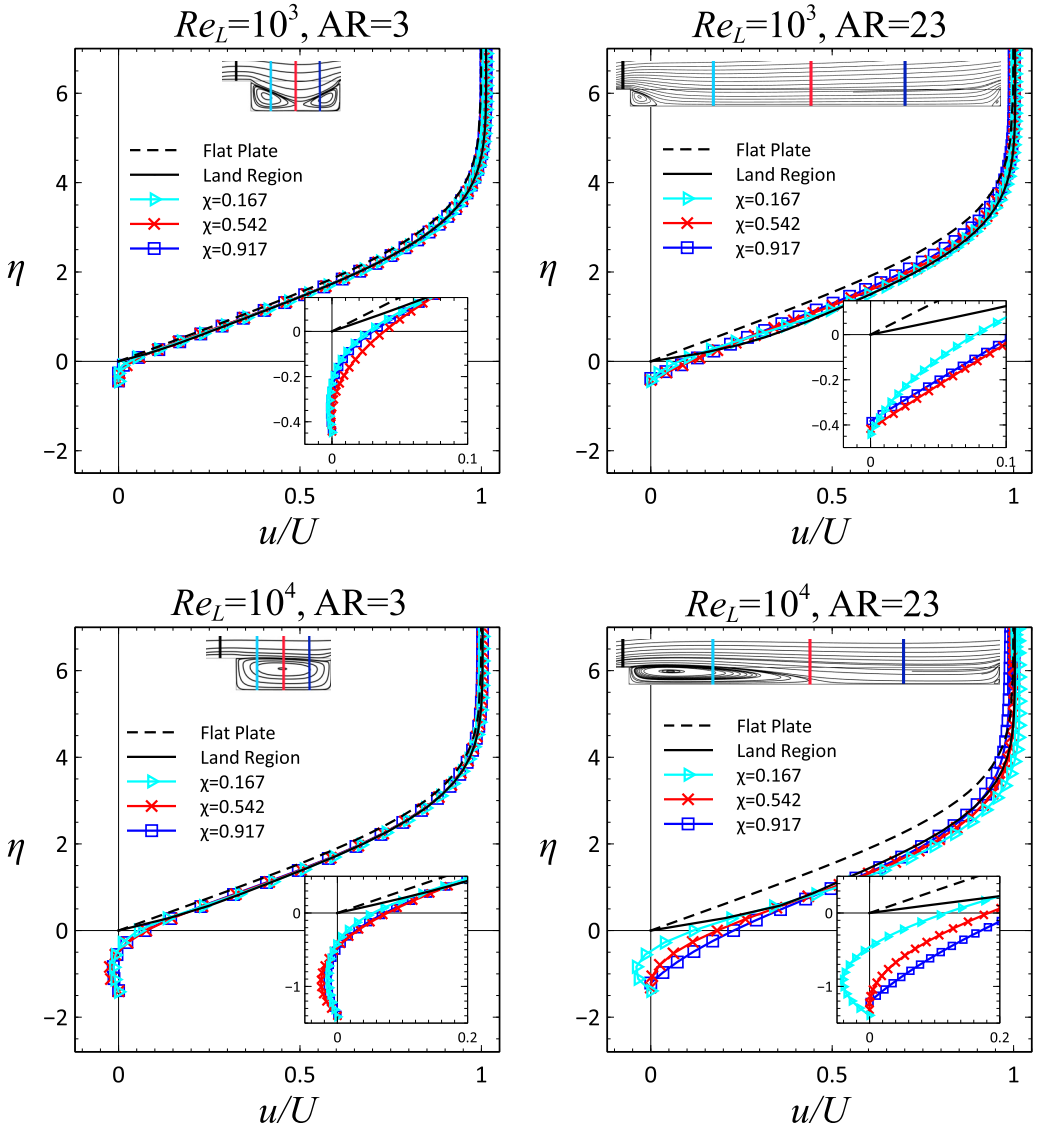

FIG. 8. Nondimensional velocity profiles at different locations along a single groove. $\eta = y/x\sqrt{\mathrm{Re}_x}$ is the similarity variable in the Blasius solution, which is extended for $y < 0$ to represent part of the profile inside the groove. Each location along the groove is distinguished by a colored line. The dashed line shows the Blasius profile of a flat plate and the solid black line corresponds to the velocity profile on the land region of a grooved plate. The negative value of u/U shows the backward motion of the fluid within the grooves due to the flow circulation.

the mainstream flow direction. For wider grooves where AR > AR*, the streamlines consist of a bigger vortex near the leading corner and a smaller one near the trailing corner. Therefore, at lower χ we can still observe a negative velocity inside the groove, whereas farther down the groove the circulation does not exist, and the main flow reaches the bottom of the trench. After this location, the velocity profile behaves similarly to a flat plate profile that starts from the bottom of the trench, and like the flat plate case, the flow exerts a positive shear on the bottom wall.

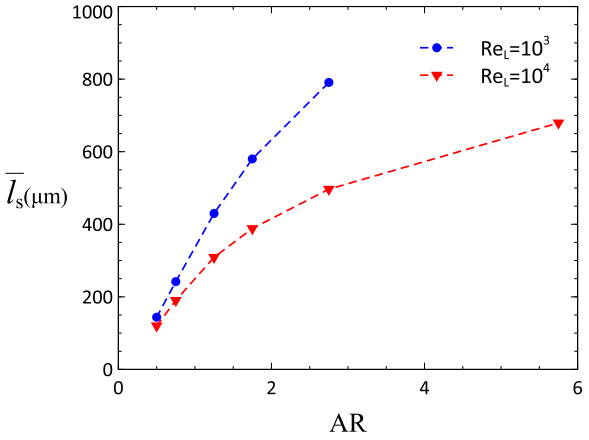

FIG. 9. Average effective slip length $\overline{l_s}$ over textured plates as a function of the grooves' aspect ratios (AR) at different global Reynolds numbers (Re_L). The slip lengths are calculated for the grooves where the free stream shows minimal bending ($AR \ll AR^*$).

C. Slippage

The performance of periodic grooves is often characterized in terms of an effective slip length. We use the Navier's slip condition and define the effective slip length over the plate as

$$\overline{l_s} = \frac{1}{L_p}\int_0^{L_p} \frac{u(x, y=0)}{(\partial u/\partial y)_{y=0}} dx, \tag{1}$$

where $\overline{l_s}$ is the average effective slip length over the plate length (L_p). We calculate the local velocity and its derivative at $y = 0$, where circulating flow inside the grooves can be distinguished from the mainstream flow. Figure 9 shows the calculated slip lengths for different ARs. We only consider the cases with $AR \ll AR^*$ to ensure that the main flow travels along the $y = 0$ line with minimal bending of the streamlines over the grooves. Close to AR^*, the streamlines deflect downward, and the interface between the main flow and the circulating flow within the grooves shifts below $y = 0$. After AR^*, as the flow reaches the bottom of the grooves, it experiences the no-slip condition at the bottom wall.

Increasing the AR with a fixed plate length creates a higher groove-to-land ratio. This means that a bigger portion of the flow is exposed to the partial slip that is provided by the grooves, which explains the increase in $\overline{l_s}$ as AR increases. Furthermore, although at higher Re_L we see larger velocities at the interface (see Fig. 8), the velocity profiles are steeper at $y = 0$. Therefore, despite showing a larger slip velocity, the magnitude of the derivatives is also larger, which causes smaller slip lengths overall. We should note that the slip length provides a measure of the skin friction reduction in comparison to the flat plate with no-slip condition. As we will show in the next sections there is a nontrivial pressure component in addition to the skin friction in transverse geometries that affects the total drag.

D. Boundary layer thickness

By extracting the velocity data over the entire domain, we can investigate the boundary layer evolution along the textures and compare it to a flat plate. For this purpose, we use the momentum thickness (θ). The momentum thickness (θ) is a measure of the momentum loss in the boundary layer relative to the inviscid flow, which can also be interpreted as a measure of the local drag force exerted on the plate. Figure 10 shows the behavior of θ along plates with different ARs at $Re_L \approx 10^4$ (please refer to the Supplemental Material for the displacement thickness plot [50]). We use the

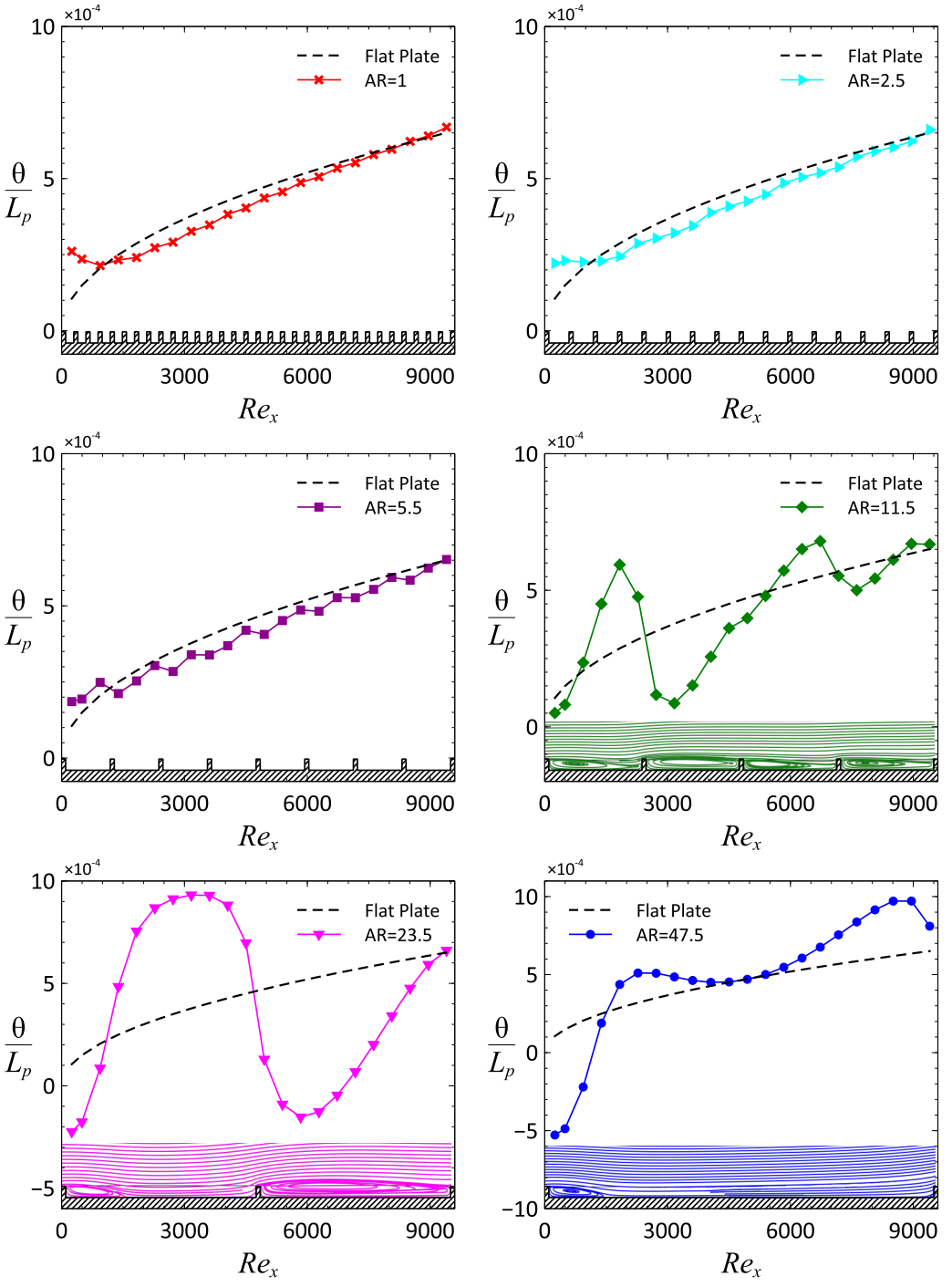

FIG. 10. Momentum thickness (θ) along the whole plate with different groove aspect ratios (AR) at global Reynolds number of $\mathrm{Re}_L \approx 10^4$. The grooves' layout associated with each AR is shown at the bottom of each plot.

local Reynolds number (Re_x) to represent the location along the plate. θ is nondimensionalized by the plate's nominal length (L_p) to enable comparison of different grooved surfaces with the flat plate. For grooves with AR $<$ AR*, because of the finite velocity and the slip-over effect of the grooves, the flow retains more of its initial momentum in the presence of the grooves in comparison to a flat plate where flow comes to a full stop at the plate's surface. Although the flow within the grooves also dissipates momentum, the order of the velocities is much smaller in comparison to the free-stream velocity. Therefore, θ is lower along the grooved plates with small ARs. While momentum reduction because of skin friction is more important for smaller ARs, at larger ARs the flow can lose part of its momentum due to stagnation at the grooves' trailing walls. This is clearly seen as an increase in θ where the flow approaches the rear wall of each groove. For AR $\sim$ AR*, the loss of momentum from one groove's trailing section is recovered by the next groove's leading section, where the pinned vortex structure lubricates and reenergizes the flow. The streamline contours at the bottom of each plot qualitatively confirm that the flow penetration in one groove is followed by formation of vortices in the next groove, which help the flow to slip over the groove despite having AR $>$ AR*. As AR further increases, the initial sharp rise at the backwall also increases, and eventually the momentum loss from the grooves with AR $\gg$ AR* can surpass the flat plate.

The difference in θ when calculated from the bottom of the grooves ($y = -C$) compared to from the interface of the groove with the main flow ($y = 0$), provides a measure of the momentum loss or gain that comes from the flow inside the grooves. We calculate this difference as $\Delta\theta = \theta(y : 0 \to H) - \theta(y : -C \to H)$, based on which a positive value indicates a gain of momentum because of the presence of the grooves in the flow. Figure 11 shows the behavior of $\Delta\theta$ along the textured plates with different ARs at $\mathrm{Re}_L = 10^4$. We see that for smaller ARs, $\Delta\theta$ is always positive, which demonstrates the role of the vortices in lubricating the movement of the free stream in textured plates as compared to a flat plate. By increasing AR, we can recognize an alternating change in the $\Delta\theta$ sign over the grooves. As AR gets closer to AR*, the flow starts to penetrate the grooves, and thus more momentum is lost because of the skin friction combined with the pressure effects of the trailing edges, which act similarly to a flap. The flow after this flap slips over the subsequent groove again. Therefore, the reduction in one groove is followed by an increase in the momentum in the following groove. However, when the plate consists of only a single groove, the reenergizing effect of the back groove is lost. Therefore, with the trailing wall acting as a Gurney flap (or wickerbill), the plate is expected to have a much larger drag as compared to a flat plate.

E. Shear and pressure evolution

Unlike streamwise textures where skin friction is the major contributor to drag, in spanwise geometries, the contribution of the pressure drag is important and should also be taken into account. Therefore, we consider individual coefficients based on the local shear and pressure within the grooves that are defined respectively as

$$C_f = \frac{\tau_w(x)}{1/2\rho U^2}, \tag{2}$$

$$C_p = \frac{\frac{1}{C}\int_{-C}^{0} P(x,y)_g dy}{1/2\rho U^2}, \tag{3}$$

where C_f is the skin friction coefficient and is calculated for horizontal segments of the textured wall by dividing the local shear stress over the free-stream dynamic pressure. C_p represents the pressure coefficient, which is calculated by averaging the local gauge pressure $[P(x,y)_g]$ along vertical lines that are equal to the groove's depth. Figure 12 shows the behavior of C_f and C_p along a textured plate with AR $= 2.5$. The C_f for a simple flat plate ($0.664/\sqrt{\mathrm{Re}_x}$) is also shown in the same plot. Transverse grooves in the plate introduce two notable changes in the trend of C_f. Firstly, the land regions show a higher shear in comparison to their corresponding location on a flat plate. This is a

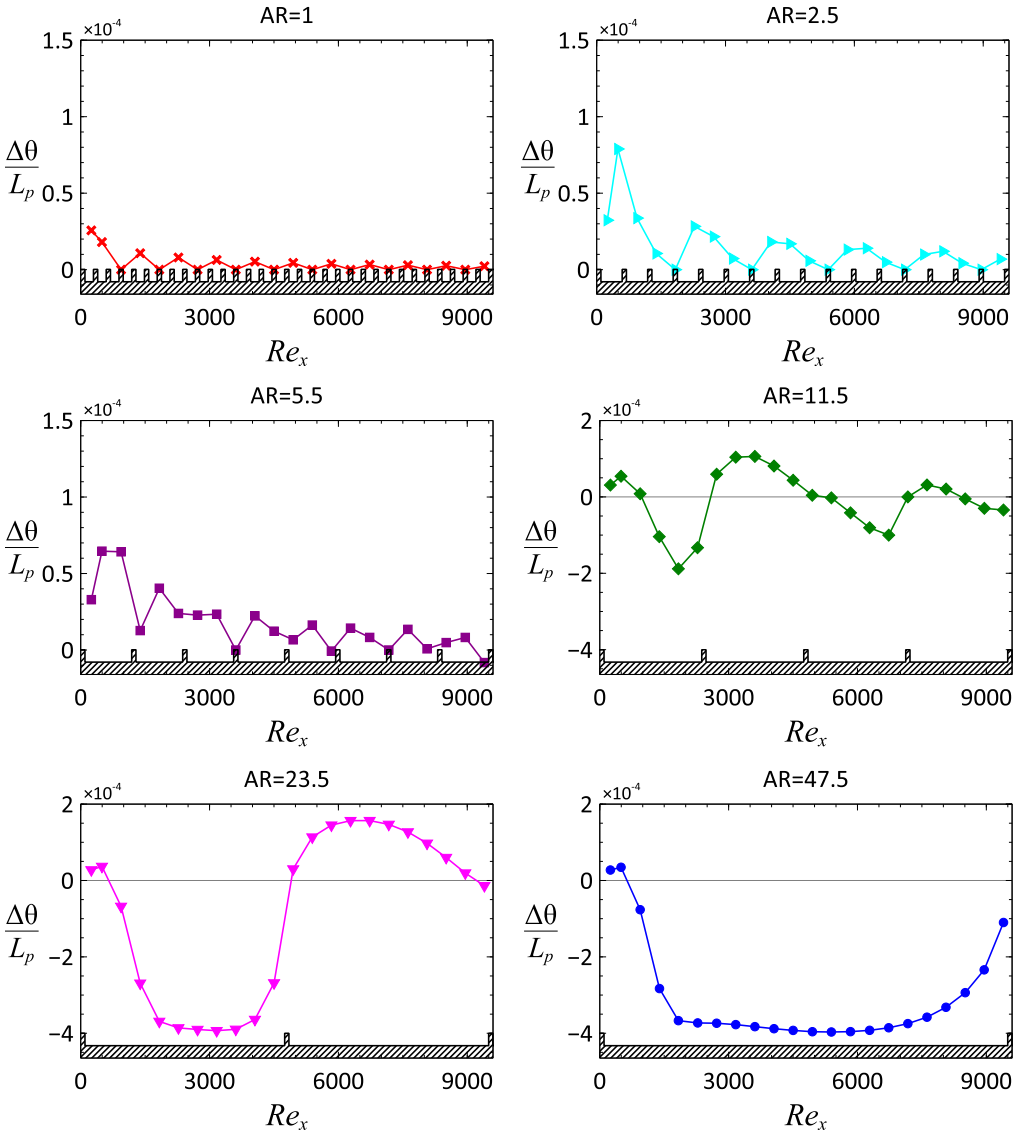

FIG. 11. The momentum thickness different ($\Delta\theta$) along textured plates with different ARs at a global Reynolds number of $\mathrm{Re}_L \approx 10^4$. The grooves' layout associated with each AR is shown at the bottom of each plot. $\Delta\theta = \theta(y:0 \to H) - \theta(y:-C \to H)$ shows the momentum gain or loss as a result of the flow in the grooves. Based on this definition, a negative value indicates a loss of momentum because of the presence of the grooves in the flow.

result of alternating between groove and land regions, where each land segment acts as a separate plate showing higher shear stresses close to its leading edge. Secondly, the flow recirculation inside each groove leads to a negative shear at the bottom of the grooves, which is favorable for drag reduction. The behavior of C_p shows a sudden reduction at the fore walls of each groove where the flow reaches the groove. The aft walls cause flow stagnation, which increases C_p and when combined with the low-pressure zones at the fore wall, causes a net drag on the wall. As the flow

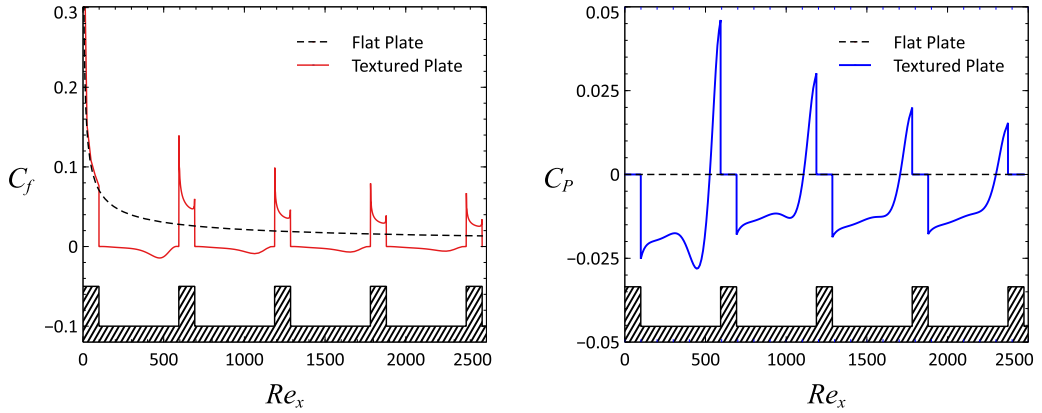

FIG. 12. The evolution of local skin friction (C_f) and pressure coefficient (C_p) along the first few trenches with aspect ratio (AR) of 2.5 at $\mathrm{Re}_L = 10^4$. The dashed line shows the local coefficients for a flat plate ($C_f = 0.664/\sqrt{\mathrm{Re}_x}$ and $C_p = 0$).

proceeds to the subsequent grooves, because of the momentum loss of the flow stream, both the peaks and valleys of the C_f and C_p curves are diminished.

The behavior of C_f and C_p inside a single groove for different ARs is shown in Fig. 13. Groove widths are scaled within zero to 1 and represented by χ to better compare the plots among different ARs. As long as AR $<$ AR*, C_f remains negative at the bottom of the groove. For AR $>$ AR*, the circulation zones are confined to the front and rear corners where the former is stronger and the latter is weaker. These corner vortices still cause an opposite shear relative to the main flow direction, which can be realized from the negative C_f at the beginning and end of the groove with AR $= 23.5$ and AR $= 47.5$. When the main flow reaches the bottom of the trench, a positive shear is exerted on the groove's wall ($C_f > 0$). Similarly, the behavior of C_p confirms the formation of an initial low-pressure zone inside the grooves shown by $C_p < 0$. C_p increases as the flow proceeds along the groove, which denotes a pressure buildup. At larger ARs, the gradual increase of C_p transitions into a sharp steplike increase in the pressure. This transition occurs when the flow hits the bottom of the grooves.

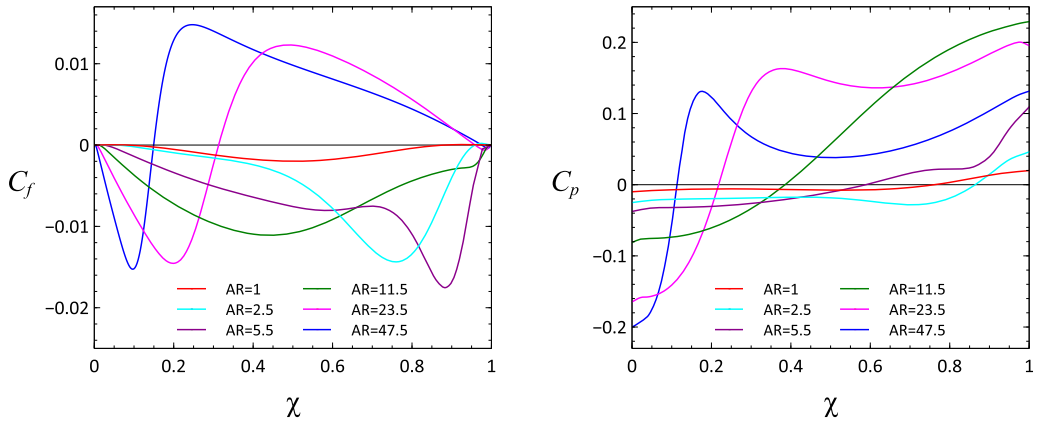

FIG. 13. Comparison of local skin friction (C_f) and pressure coefficient (C_p) in a single trench for different aspect ratios (AR). χ represents a normalized length scale for the grooves, projecting the different grooves' widths between zero and 1.

F. Skin, pressure, and total drag

We can calculate the global effect of both pressure and skin friction on drag by using the local pressure and shear stress from the simulations. The skin friction drag is a result of the flow shear that acts tangentially on the wall. In addition, we see that in transverse configurations, low-pressure zones form at the leading edge followed by high-pressure stagnation zones at the trailing edge of each trench, causing a net pressure force on the plate. Ultimately, we define a total drag coefficient based on which we can compare the drag reduction effectiveness among grooves with different ARs and flow conditions. For each component, we define the average drag coefficients as

$$\overline{C_f} = \frac{F_f}{\frac{1}{2}\rho U^2 L_p} = \frac{\int_0^{L_w} [\hat{n}.\hat{\tau}]_w.\hat{x}dL}{\frac{1}{2}\rho U^2 L_p}, \tag{4}$$

$$\overline{C_p} = \frac{F_p}{\frac{1}{2}\rho U^2 L_p} = \frac{\int_0^{L_w} -[\hat{n}.pI]_w.\hat{x}dL}{\frac{1}{2}\rho U^2 L_p}. \tag{5}$$

Each coefficient is determined by calculating the corresponding local stress, namely, shear ($\tilde{\tau}$) and pressure (pI) at the wall, and integrating the projected stress in the drag direction (x direction) along the wetted wall (L_w). L_w shows the total length of the wetted wall including the dimensions of the grooves, whereas L_p represents the nominal plate length (for a flat plate $L_p = L_w$). For the cases that show unsteady behavior, we perform a second integration over time to calculate the average drag coefficients.

Before comparing the drag properties among all the cases, it is worth briefly discussing the effects of unsteadiness on the drag components. Figure 14 shows the transient behavior of the flow over the whole plate for two different cases and their corresponding drag coefficients. We can notice a series of moving vortices traveling in the flow direction. As discussed earlier, at smaller ARs, these vortices are confined to the grooved regions, displaying a repeating motion pattern within them that results in a periodic oscillation in pressure and skin friction coefficients as seen in Fig. 14(a). In this case, the vortices inside the grooves may still, on average, provide a lower drag as compared to a flat plate. However, at larger ARs, the flow loses a substantial amount of its momentum during the vortex interaction with the trailing wall of the groove which acts as a blunt body and leads to vortex shedding, with the vortex leaving the groove region and traveling downstream in the main flow. In this state, both drag coefficients become more erratic with time as shown in Fig. 14(b), and the overall drag increases substantially.

Figure 15 compares the skin friction and pressure drag coefficients for different trench geometries at $\mathrm{Re}_L \approx 10^4$. Different groove configurations are characterized by AR and $\varepsilon = C/L_p$. The simulations are performed for a wide range of trench aspect ratios, from deep trenches (AR = 0.25) to shallow trenches (AR = 192), and at four different roughness values. The presence of steady vortices inside the grooves causes the main flow to partially slip over the trench region at low ARs, which results in reduction of the skin friction. Increasing AR in the simulations corresponds to decreasing the number of grooves and land regions, while increasing the groove-to-land ratio (B/A). As B/A increases, a bigger portion of the flow is exposed to the slip condition provided by the grooves. Furthermore, because the number of land regions is reduced, fewer spikes form in the shear stress evolution, as seen in Fig. 12; this further reduces the skin friction. At larger ARs, higher deflection of the streamlines eventually causes the primary circulation inside the grooves to collapse. In this situation since the main vortex is not sustained, the shear-reducing effect of the trenches is limited to the smaller vortices at the front and back corners, and the flow exerts positive shear force on most of the groove's bottom wall. Thus, skin friction starts to increase. Very shallow trenches essentially represent multiple flat surfaces separated by a few bumps. Ultimately, as AR $\rightarrow \infty$, the value of the friction coefficient asymptotically reaches the flat plate coefficient ($\bar{C}_f = 1.328/\sqrt{\mathrm{Re}_L} \approx 0.0136$). On the other end, as AR $\rightarrow$ 0, the

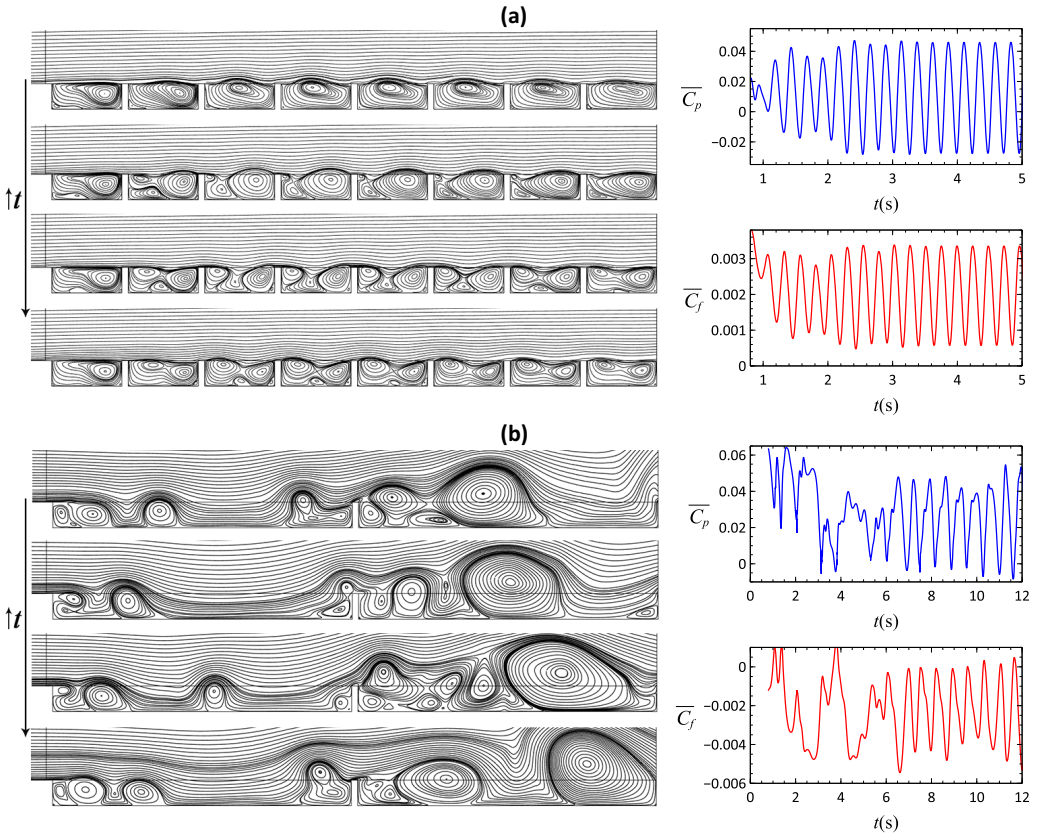

FIG. 14. Transient behavior of the streamlines over the whole grooved plate and their corresponding fluctuation in the drag coefficients. (a) At smaller AR, the transient vortices are confined within the grooves and both skin friction and pressure coefficients show a periodic trend. In this situation, the time-averaged total drag coefficient is still lower than a flat plate. (b) At larger AR, interaction of the flow with the trailing wall of the groove that act as a blunt body, causes oscillations in the flow similar to a vortex shedding phenomenon. During this process the flow loses a significant portion of its momentum and as a consequence, the plate experiences a much higher drag in comparison to a flat plate.

plate mostly consists of land segments and the overall skin drag will approach the flat plate again.

The pressure drag coefficient behaves almost opposite to the skin friction drag. The permanent, circulating flow inside the grooves at low ARs is able to lift the external flow on top of the grooves such that the streamlines do not feel the vertical walls of the grooves as they travel over the textures. In this state, the pressure effects are mainly concentrated near the top corners of the grooves. The high-pressure regions forming at the trailing wall of one groove combined with the low-pressure zone at the leading wall of the subsequent groove causes a net pressure drag force. Here, on the one hand, increasing the AR enhances the flow penetration into the grooves, which causes the grooves' vertical walls to act similarly to a flap in the flow. On the other hand, in a fixed plate length, a larger AR corresponds to fewer grooves and thus fewer flaps. Therefore, there is a trade-off between the number of grooves in the plate and their pressure effects, which results in a maximum for $\bar{C}_p$. We can make similar arguments for AR $\to 0$ or AR $\to \infty$, where $\bar{C}_p$ approaches zero toward both ends as in the case of a flat surface. We should note that, for grooves in which flow oscillations occur, the presence of unsteady vortices typically causes substantial increase in the pressure drag, which can be observed for $\varepsilon = 0.04$ in Fig. 15(b).

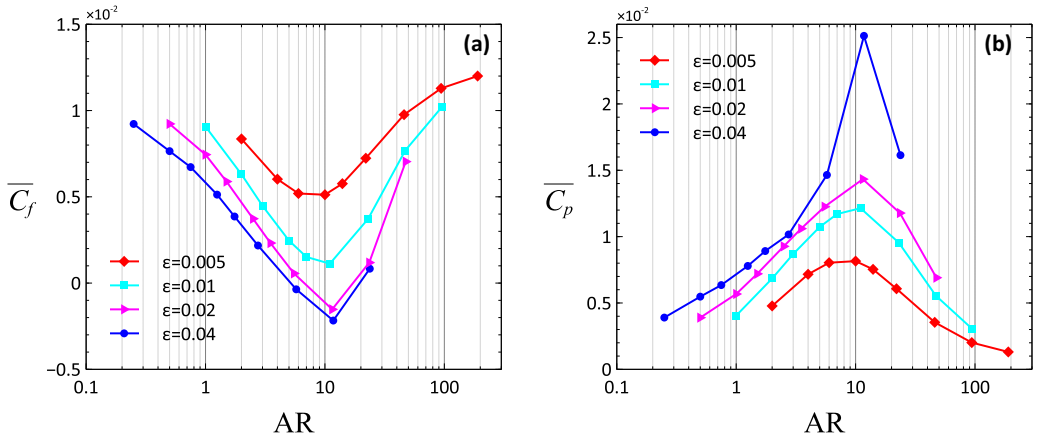

FIG. 15. (a) Average skin friction coefficient ($\bar{C}_f$) and (b) average pressure coefficient ($\bar{C}_p$) over the whole textured plate with different groove aspect ratios (AR) and roughness values ($\varepsilon = C/L_p$) at $\mathrm{Re}_L \approx 10^4$.

The two drag components obtained in the previous section constitute the total drag coefficient, which is simply defined as

$$\overline{C_D} = \frac{F_D}{\frac{1}{2}\rho U^2 L_p} = \frac{F_f + F_p}{\frac{1}{2}\rho U^2 L_p}. \tag{6}$$

To better appreciate the drag-reducing or -increasing effect of the grooves, we plot the total drag coefficient change (ΔC_D) in comparison to a flat plate (C_{D0}) in Fig. 16. Negative values of $\Delta C_D/C_{D0}$ denote a reduction, while positive values denote an increase in the total drag compared to a flat plate of the same length. Groove geometries with smaller ARs reduce the total drag despite having a larger wetted area, as the reduction in skin friction is higher than the increase caused by the pressure drag. At smaller ε we see that drag reduction gradually decreases. Since the pressure drag acts on shorter

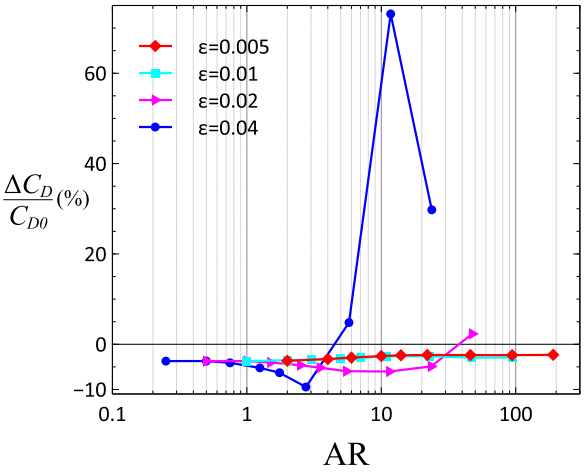

FIG. 16. Percentage reduction of total drag coefficient for different aspect ratios (AR) and roughness values (ε) at $\mathrm{Re}_L \approx 10^4$. ΔC_D is the signed difference of the drag coefficient of a grooved plate and a flat surface, and C_{D0} is the total drag coefficient of a flat plate ($C_{D0} = \bar{C}_f = 1.328/\sqrt{\mathrm{Re}_L}$). The negative values represent drag reduction, while the positive values show drag increase in comparison to a flat plate of the same nominal length.

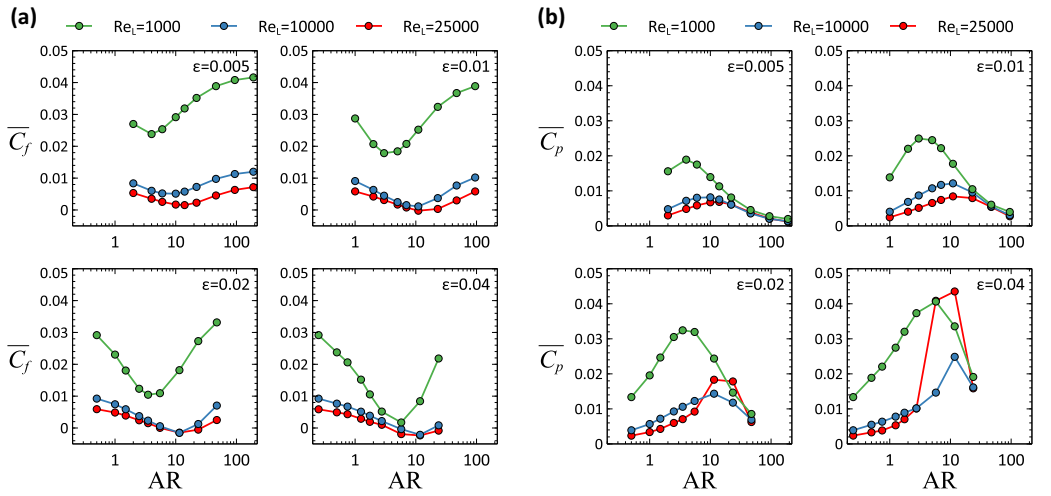

FIG. 17. Comparison of (a) average skin friction coefficient ($\bar{C}_f$) and (b) average pressure coefficient ($\bar{C}_p$) for different aspect ratios (AR) and roughness values (ε) at three different global Reynolds numbers (Re_L). We can generally notice valley-shaped plots for $\bar{C}_f$ and bell-shaped behavior for $\bar{C}_p$, indicating their opposite effects in the total drag. Presence of the grooves allows for creation of vortices which help with drag reduction by reducing skin friction. However, the vertical walls of each groove act like blunt bodies in the flow, causing a net pressure force, thus increasing the drag.

vertical walls, their increasing action can still be compensated by the reduction in skin friction that is achieved at the front and rear corners of each groove. For grooves with bigger ε, we notice an initial increase in drag reduction followed by a sharp decrease in the trend. Here as AR increases, pressure forces act on larger surface areas at the front and rear walls, which eventually surpass the reduction in the skin fiction by the corner vortices. Consequently, this leads to an overall drag force much higher than the flat plate without any textures.

To get an overall view of the effect of transverse grooves at different Re_L, we plot the drag coefficients for each ε in a separate plot with respect to AR at different Re_L in Fig. 17. The overall valley-shaped behavior of skin friction and bell-shaped behavior of pressure drag can be observed at different Re_L. However, we see that the minimum and maximum of the $\bar{C}_f$ and $\bar{C}_p$ graphs, respectively, shift toward larger AR, which indicates an increase in the value of AR*. By increasing Re_L, both drag coefficients decline, and their overall shape transitions to a flatter curve. We should note that presence of the grooves results in lower $\bar{C}_f$ at all the tested Re_L compared to their corresponding flat surface skin friction. However, unlike a flat surface with zero-pressure drag, transverse grooves in the flow always result in positive $\bar{C}_p$.

Finally, we plot the total drag reduction (*DR*) in Fig. 18. *DR* is defined as $(F_D - F_{D0})/F_{D0}$ where F_D and F_{D0} represent the total drag force of the grooved plate and the flat plate, respectively. In this sense, *DR* and $\Delta C_D/C_{D0}$ have equal values for each case. The trade-off between skin friction reduction and the pressure drag increase at different Re_L creates distinct behaviors for different ε. We can see that at smaller ε, *DR* remains negative for all the AR and Re_L, which indicates that in such grooves the decrease in skin friction overcomes the increase in pressure drag. Moreover, we can notice that in general, smaller AR performs slightly better at lower Re_L. Increasing AR can have significantly different effects on the drag. For smaller ε, the drag gradually increases, whereas, for bigger ε, it initially decreases. However, further increase in AR for bigger ε causes a quick rise in the drag, as a result of the substantial increase in the pressure drag, which becomes worse with the unsteady fluctuation of vortices over the grooves. It is therefore extremely important to choose the appropriate groove dimensions depending on the overall flow conditions of the system. The results

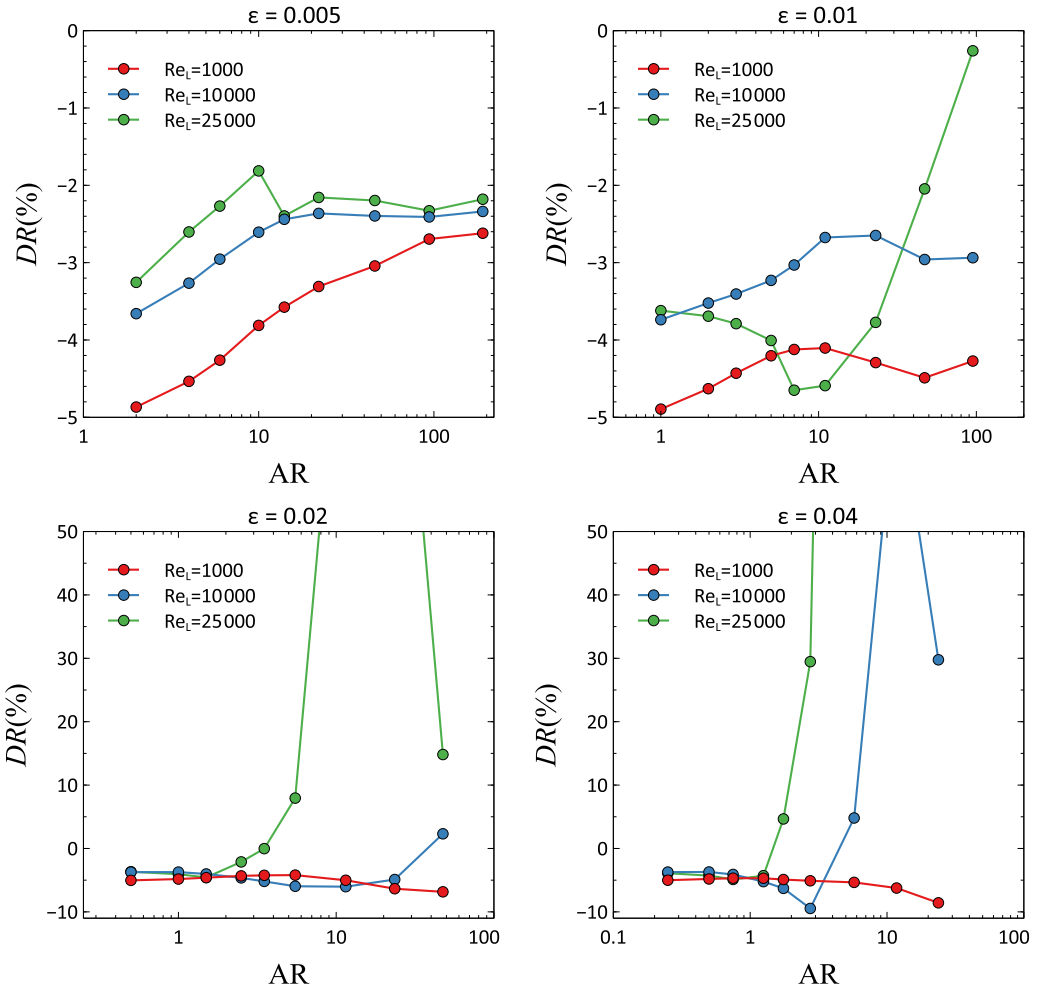

FIG. 18. Comparison of the total drag reduction (DR) over the grooved surfaces with different groove aspect ratios (AR) and global Reynolds numbers (Re_L). Each plot represents a different roughness value ($\varepsilon = C/L_p$).

show a drag reduction as low as 10% for the range of the flow conditions and groove dimensions simulated in this study.

V. CONCLUSIONS

In this paper, we have studied drag characteristics of periodic spanwise grooves in incompressible viscous laminar flows. The grooves have rectangular cross sections, which are characterized by their width-to-depth aspect ratio ($\mathrm{AR} = B/C$), and a relative roughness that shows the ratio of the grooves' depth to the plate's nominal length ($\varepsilon = C/L_p$). We have used numerical simulations to study the pressure and velocity fields over the plate and to investigate the evolution of boundary layer along the grooves. We defined a critical aspect ratio, denoted by AR^*, to distinguish the flow behavior of the grooves. The presence of transverse grooves in the flow results in vortical flow structures inside the grooves. Specifically, when $\mathrm{AR} < \mathrm{AR}^*$ the grooves are filled with permanent steady circulations, which are able to sustain the main flow that is traveling on top of them. By

creating a partial slip condition above the grooves, such vortices facilitate flow movement over the plate and result in a lower skin friction in comparison to a flat plate. An inevitable consequence of spanwise grooves is the emergence of the pressure drag. The interaction of flow with vertical walls of the grooves results in a net pressure force. The increase in pressure drag and the reduction in skin friction lead to a trade-off in the total drag, which ultimately determine the grooves drag-reducing or even -increasing effects, as compared to a flat surface. When $AR > AR^*$, the free stream penetrates the grooves. With the main flow reaching the bottom of the grooves, the effect of the vortices is mainly confined to the grooves' corners, whereas the flow exerts shear to most of the bottom surface. Moreover, as the flow travels to the subsequent groove, the vertical walls that separate each two grooves behave as a block to the main flow, which adds a substantial pressure drag. Therefore, the total drag may even increase in comparison to a flat plate. As grooves get deeper (larger ε), the action of vertical walls as a blunt body becomes more pronounced. At higher Re_L, the flow interaction with deeper grooves causes unsteady flow behaviors, namely, vortex shedding, which further increases the total drag. With careful design of the groove dimensions at different flow conditions, transverse grooves can provide a net drag reduction despite increasing the wetted area of the plate. The numerical results show that a total drag reduction of about 10% can be obtained in the laminar regime. The trench profiles can be optimized in future studies to reduce the adverse pressure effects while maintaining the interior circulations to create further drag reductions. Moreover, the introduction of these transverse grooves may even result in delaying the laminar-to-turbulent transition, by reducing the overall momentum thickness along the surface, which is worth studying in future works. Similarly, a combination of different texture configurations (e.g., streamwise and herringbone geometries) can be used in conjunction with transverse geometries to provide an optimum solution to drag reduction for a wide range of flow conditions in both laminar and turbulent regimes.

ACKNOWLEDGMENTS

The funding for this work was granted by the National Science Foundation (NSF), Award No. 1705958. The authors wish to thank John Healy for helping with the simulations.

[1] N. S Berman, Drag reduction by polymers, Annu. Rev. Fluid Mech. **10**, 47 (1978).
[2] J. L. Lumley, Drag reduction by additives, Annu. Rev. Fluid Mech. **1**, 367 (1969).
[3] G. Yunqing, L. Tao, M. Jiegang, S. Zhengzan, and Z. Peijian, Analysis of drag reduction methods and mechanisms of turbulent, Appl. Bionics Biomech. **2017**, 6858720 (2017).
[4] H. A. Abdulbari, H. D. Mahammed, and Z. B. Y. Hassan, Bio-inspired passive drag reduction techniques: A review, ChemBioEng Rev. **2**, 185 (2015).
[5] R. Handler and L. Sirovich, Direct numerical simulation of turbulent flow over a modelled riblet covered surface, J. Fluid Mech. **302**, 333 (1995).
[6] F. E. Fish and G. V. Lauder, Passive and active flow control by swimming fishes and mammals, Annu. Rev. Fluid Mech. **38**, 193 (2006).
[7] C. Lee, C. H. Choi, and C. J. Kim, Superhydrophobic drag reduction in laminar flows: A critical review, Exp. Fluids **57**, 176 (2016).
[8] P. Roach, N. J. Shirtcliffe, and M. I. Newton, Progess in superhydrophobic surface development, Soft Matter **4**, 224 (2008).
[9] T. J. Kim, R. Kanapuram, A. Chhabra, and C. Hidrovo, Thermo-wetting and friction reduction characterization of microtextured superhydrophobic surfaces, J. Fluids Eng. **134**, 114501 (2012).
[10] A. B. D. Cassie and S. Baxter, Wettability of porous surfaces, Trans. Faraday Soc. **40**, 546 (1944).
[11] B. R. Solomon, K. S. Khalil, and K. K. Varanasi, Drag reduction using lubricant-impregnated surfaces in viscous laminar flow, Langmuir **30**, 10970 (2014).

[12] M. S. Bobji, S. V. Kumar, A. Asthana, and R. N. Govardhan, Underwater sustainability of the "Cassie" state of wetting, Langmuir **25**, 12120 (2009).
[13] E. Alinovi and A. Bottaro, Apparent slip and drag reduction for the flow over superhydrophobic and lubricant-impregnated surfaces, Phys. Rev. Fluids **3**, 124002 (2018).
[14] Z. Ge, H. Holmgren, M. Kronbichler, L. Brandt, and G. Kreiss, Effective slip over partially filled microcavities and its possible failure, Phys. Rev. Fluids **3**, 054201 (2018).
[15] J. Kadoko, G. Karamanis, T. Kirk, and M. Hodes, One-dimensional analysis of gas diffusion-induced Cassie to Wenzel state transition, J. Heat Transfer **139**, 122006 (2017).
[16] N. A. Patankar, Vapor stabilizing substrates for superhydrophobicity and superslip, Langmuir **26**, 8783 (2010).
[17] D. Dilip, N. K. Jha, R. N. Govardhan, and M. S. Bobji, Controlling air solubility to maintain "Cassie" state for sustained drag reduction, Colloids Surf., A **459**, 217 (2014).
[18] T. J. Kim and C. Hidrovo, Pressure and partial wetting effects on superhydrophobic friction reduction in microchannel flow, Phys. Fluids **24**, 112003 (2012).
[19] D. Schäffel, K. Koynov, D. Vollmer, H. J. Butt, and C. Schönecker, Local Flow Field and Slip Length of Superhydrophobic Surfaces, Phys. Rev. Lett. **116**, 134501 (2016).
[20] G. Bolognesi, C. Cottin-Bizonne, and C. Pirat, Evidence of slippage breakdown for a superhydrophobic microchannel, Phys. Fluids **26**, 082004 (2014).
[21] M. J. Walsh and L. M. Weinstein, Drag and heat-transfer characteristics of small longitudinally ribbed surfaces, AIAA J. **17**, 770 (1979).
[22] M. Walsh, Turbulent boundary layer drag reduction using riblets, in *Proceedings of the 20th Aerospace Sciences Meeting* (American Institute of Aeronautics and Astronautics, Reston, VA, 1982).
[23] M. Walsh and A. Lindemann, Optimization and application of riblets for turbulent drag reduction, in *Proceedings of the 22nd Aerospace Sciences Meeting* (American Institute of Aeronautics and Astronautics, Reston, VA, 1984).
[24] B. Dean and B. Bhushan, Shark-skin surfaces for fluid-drag reduction in turbulent flow: A review, Philos. Trans. R. Soc., A **368**, 4775 (2010).
[25] G. D. Bixler and B. Bhushan, Fluid drag reduction with shark-skin riblet inspired microstructured surfaces, Adv. Funct. Mater. **23**, 4507 (2013).
[26] H. Choi, P. Moin, and J. Kim, Direct numerical simulation of turbulent flow over riblets, J. Fluid Mech. **255**, 503 (1993).
[27] S. J. Lee and S. H. Lee, Flow field analysis of a turbulent boundary layer over a riblet surface, Exp. Fluids **30**, 153 (2001).
[28] G. D. Bixler and B. Bhushan, Shark skin inspired low-drag microstructured surfaces in closed channel flow, J. Colloid Interface Sci. **393**, 384 (2013).
[29] L. Djenidi, F. Anselmet, J. Liandrat, and L. Fulachier, Laminar boundary layer over riblets, Phys. Fluids **6**, 2993 (1994).
[30] S. Raayai-Ardakani and G. H. McKinley, Drag reduction using wrinkled surfaces in high Reynolds number laminar boundary layer flows, Phys. Fluids **29**, 093605 (2017).
[31] J. P. Rothstein, Slip on superhydrophobic surfaces, Annu. Rev. Fluid Mech. **42**, 89 (2010).
[32] J. Ou, B. Perot, and J. P. Rothstein, Laminar drag reduction in microchannels using ultrahydrophobic surfaces, Phys. Fluids **16**, 4635 (2004).
[33] C. C. Mei and X. Y. Guo, Numerical study of laminar boundary-layer flows over a superhydrophobic plate, Phys. Fluids **30**, 072002 (2018).
[34] Y. Huang, X. Zhao, Y. Pan, and K. Ahmad, Simulation of effective slip and drag in pressure-driven flow on superhydrophobic surfaces, J. Nanomater. **2016**, 5052602 (2016).
[35] J. Davies, D. Maynes, B. W. Webb, and B. Woolford, Laminar flow in a microchannel with superhydrophobic walls exhibiting transverse ribs, Phys. Fluids **18**, 087110 (2006).
[36] P. F. Hao, C. Wong, Z. H. Yao, and K. Q. Zhu, Laminar drag reduction in hydrophobic microchannels, Chem. Eng. Technol. **32**, 912 (2009).
[37] E. Celia, T. Darmanin, E. Taffin de Givenchy, S. Amigoni, and F. Guittard, Recent advances in designing superhydrophobic surfaces, J. Colloid Interface Sci. **402**, 23647693 (2013).

[38] G. Daschiel, M. Perić, J. Jovanović, and A. Delgado, The holy grail of microfluidics: Sub-laminar drag by layout of periodically embedded microgrooves, Microfluid. Nanofluid. **15**, 675 (2013).
[39] A. Gaddam, B. S. Kattemalalawadi, A. Agrawal, and S. S. Joshi, Demarcating wetting states in textured microchannels under flow conditions by Poiseuille number, Microfluid. Nanofluid. **21**, 137 (2017).
[40] C. W. Rowley and D. R. Williams, Dynamics and control of high-Reynolds-number flow over open cavities, Annu. Rev. Fluid Mech. **38**, 251 (2005).
[41] Sutardi and C. Y. Ching, Effect of different sized transverse square grooves on a turbulent boundary layer, Exp. Fluids **34**, 261 (2003).
[42] C. W. Rowley, T. Colonius, and A. J. Basu, On self-sustained oscillations in two-dimensional compressible flow over rectangular cavities, J. Fluid Mech. **455**, 315 (2002).
[43] G. A. Brés and T. Colonius, Three-dimensional instabilities in compressible flow over open cavities, J. Fluid Mech. **599**, 309 (2008).
[44] V Sarohia, Experimental and analytical investigation of oscillations in flows over cavities, Ph.D. thesis, California Institute of Technology, 1975.
[45] T. B. Gatski and C. E. Grosch, Embedded cavity drag in steady laminar flow, AIAA J. **23**, 1028 (1985).
[46] H. Chen, Y. Gao, H. A. Stone, and J. Li, "Fluid bearing" effect of enclosed liquids in grooves on drag reduction in microchannels, Phys. Rev. Fluids **1**, 083904 (2016).
[47] A. Vuddagiri and A. Samad, Vortex trapping by different cavities on an airfoil, Wind Eng. **37**, 469 (2013).
[48] W. F. J. Olsman, J. F. H. Willems, A. Hirschberg, T. Colonius, and R. R. Trieling, Flow around a NACA0018 airfoil with a cavity and its dynamical response to acoustic forcing, Exp. Fluids **51**, 493 (2011).
[49] S. Zhang, X. Ouyang, J. Li, S. Gao, S. Han, L. Liu and H. Wei, Underwater drag-reducing effect of superhydrophobic submarine model, Langmuir **31**, 587 (2015).
[50] See Supplemental Material at http://link.aps.org/supplemental/10.1103/PhysRevFluids.5.064102 for a discussion of transient and steady simulation conditions, three-dimensional model verification, and displacement thickness plot.
[51] H. Yao, R. K. Cooper, and S. Raghunathan, Numerical simulation of incompressible laminar flow over three-dimensional rectangular cavities, J. Fluids Eng. **126**, 919 (2005).
[52] H. K. Moffatt, Viscous and resistive eddies near a sharp corner, J. Fluid Mech. **18**, 1 (1964).
[53] J. E. Rossiter, Wind tunnel experiments on the flow over rectangular cavities at subsonic and transonic speeds, RAE Technical Report No. 64037 (Ministry of Aviation, Royal Aircraft Establishment, RAE Farnborough, UK, 1964).